Plasmonic Enhancement of Dye Sensitized Solar Cells in the Red-to-near-Infrared Region using Triangular Core−Shell Ag@SiO₂ Nanoparticles

Mahesh K. Gangishetty,[†] Kee Eun Lee,[†] Robert W. J. Scott, and Timothy L. Kelly*

Department of Chemistry, University of Saskatchewan, 110 Science Place, Saskatoon, Saskatchewan, S7N 5C9, Canada

Ⓢ Supporting Information

ABSTRACT: Recently, plasmonic metal nanoparticles have been shown to be very effective in increasing the light harvesting efficiency (LHE) of dye-sensitized solar cells (DSSCs). Most commonly, spherical nanoparticles composed of silver or gold are used for this application; however, the localized surface plasmon resonances of these isotropic particles have maxima in the 400−550 nm range, limiting any plasmonic enhancements to wavelengths below 600 nm. Herein, we demonstrate that the incorporation of anisotropic, triangular silver nanoprisms in the photoanode of DSSCs can dramatically increase the LHE in the red and near-infrared regions. Core−shell Ag@SiO₂ nanoprisms were synthesized and incorporated in various quantities into the titania pastes used to prepare the photoanodes. This optimization led to an overall 32 ± 17% increase in the power conversion efficiency (PCE) of cells made using 0.05% (w/w) of the Ag@SiO₂ composite. Measurements of the incident photon-to-current efficiency provided further evidence that this increase is a result of improved light harvesting in the red and near-infrared regions. The effect of shell thickness on nanoparticle stability was also investigated, and it was found that thick (30 nm) silica shells provide the best protection against corrosion by the triiodide-containing electrolyte, while still enabling large improvements in PCE to be realized.

KEYWORDS: plasmonics, dye sensitized solar cells, metal nanoparticles, light trapping, Ag@SiO₂, silver nanoprisms
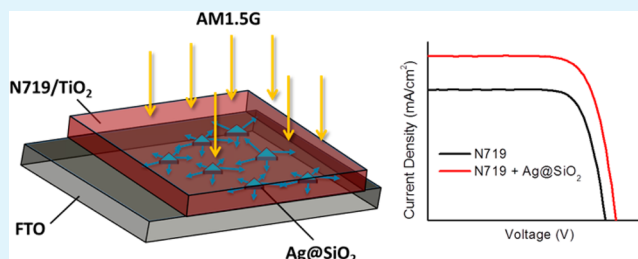
INTRODUCTION

Dye-sensitized solar cells (DSSCs) have attracted a great deal of scientific and technical interest because of their low cost and ease of fabrication. While the development of new dyes has led to continued improvements in the power conversion efficiencies (PCEs) of DSSCs in recent years,[1] they are still often limited by the weak absorption of the dye sensitizer. This is exemplified by the commonly used ruthenium(II) poly-pyridyl dyes (e.g., N719). N719 absorbs strongly at 535 nm, but has drastically reduced extinction coefficients at longer wavelengths.[2] Thus, improving the light harvesting efficiency (LHE) in the 600−900 nm wavelength range is one promising way of increasing the PCEs of these devices.[3,4] The synthesis of panchromatic sensitizers, such as porphyrin derivatives, has been shown to improve the incident photon-to-current efficiency (IPCE) at longer wavelengths;[5,6] however, the overall efficiency of these dyes is often lower than champion ruthenium dyes because of their reduced LHE at shorter wavelengths.

This issue of poor light absorption often necessitates the use of thick photoanodes,[7] scattering layers,[8−10] back reflectors,[11] or other light trapping elements[12] to achieve the LHE required to produce a highly efficient DSSC. An emerging approach to better light harvesting in solar cells utilizes the localized surface plasmon resonances (LSPRs) of noble metal nanostructures

(e.g., Au or Ag).[13,14] Because of their unique optical properties, plasmonic nanoparticles are finding applications in diverse scientific fields such as catalysis,[13] electronics,[14] biological imaging,[15] and sensing.[16] When applied to a DSSC, the plasmonic nanoparticles can act as efficient light trapping components, resulting in an enhancement of the LHE of the cell.[17−23] Plasmonic materials can enhance the LHE in one of several ways. The first is by resonant scattering of the incident light, whereby incident light is scattered off-normal, increasing the effective optical path length of the device. Another possibility is that the excitation of LSPR modes greatly increases the local electric field at the particle surface (near-field enhancement), and that this results in an increase of the absorbance of the dye sensitizer in these regions.

A number of approaches have been explored for the incorporation of metal nanoparticles in a DSSC. In the simplest of these, gold nanoparticles were directly mixed with the TiO₂ nanoparticle paste, resulting in Au/TiO₂ composite electrodes.[18] These electrodes produced a substantial increase in the current density generated at 532 nm, near the absorption maximum of the gold LSPR. Similarly, an increase in the short

circuit current density was observed when silver nanoparticles were embedded in the photoanode of a DSSC by an in situ synthetic procedure.[22] Despite these promising results, the use of bare metal nanoparticles is undesirable from a stability perspective, because the bare nanoparticles may suffer from surface corrosion when in direct contact with the dye and iodide/triiodide electrolyte.[24] The nanoparticles may also act as electron traps, reducing the electron collection efficiency. To remedy this, the use of core−shell nanoparticles has been explored, where the plasmonic core is protected by a thin metal oxide (e.g., SiO_2, TiO_2) shell.[19,20] The insulating shell both protects the underlying particle from oxidative etching and also helps prevent unwanted electron storage effects.[25] The effect of multiple shells and particle aggregation has also been explored through the synthesis of Au@SiO_2@TiO_2 nanoparticles.[26]

Most of these studies on plasmon-enhanced DSSCs have been based on spherical nanoparticles, and the maxima of the LSPR bands for these materials typically lie in the range of 400−550 nm.[19,20] Conventional ruthenium dyes such as N719 already absorb strongly in these regions, diminishing the need for plasmonic light trapping. In contrast, N719 absorbs much more weakly in the 550−700 nm range, and to better amplify the LHE in this regime, better spectral match between the LSPR band and the edge of the N719 absorption band is required. The position of the LSPR band depends on factors such as the nanoparticle size, shape, and dielectric environment.[27] While spherical silver nanoparticles typically have LSPR absorption bands in the range of 380−450 nm, anisotropic nanoparticles such as triangular silver nanoprisms have substantially red-shifted extinction maxima. By changing the aspect ratio of the silver nanoprisms, the position of the LSPR band can be tuned anywhere from the blue-violet to the near-infrared (NIR) region of the spectrum.[28] Gold nanorods[29] and silver nanoprisms[30] have both demonstrated the viability of such an approach in polymer bulk heterojunction solar cells.

In this study, we synthesize core−shell nanoparticles consisting of a triangular silver nanoprism core and a silica shell of variable thickness (Ag@SiO_2). The core−shell particles display a broad LSPR band centered at about 730 nm, which is ideally suited to overlap with the edge of the N719 absorption spectrum. The silica coating was designed to both protect the underlying silver nanoprism from the corrosive I^-/I_3^- redox mediator and prevent electron transfer from either the TiO_2 or the dye excited state to the metal nanoparticle. We find that the incorporation of 0.05% (w/w) Ag@SiO_2 into the photoanode of a DSSC results in a 32 ± 17% increase in the overall PCE of the device, and that this improvement is entirely driven by an increase in the short circuit current density. IPCE measurements suggest that this is due to an improvement in LHE in the 550−750 nm range, caused by plasmonic light trapping effects.

EXPERIMENTAL SECTION

Materials. Silver nitrate (99%), sodium borohydride (98%), and hydrogen peroxide (30% w/w), glacial acetic acid (99.7%), nitric acid (70%), and iso-propanol (99.9%) were purchased from Fisher Scientific. Ethyl cellulose (EC) powders EC-10 (Ethocel standard 10 cP) and EC-45 (Ethocel standard 45 cP) were purchased from Dow Chemicals. α-Terpineol (≥96%), sodium citrate tribasic (≥96%), poly(N-vinylpyrrolidone) (≥99%, MW ~ 40,000), 16-mercaptohexadecanoic acid (90%), tetraethoxysilane (99%), titanium tetraisopropoxide (≥97%), and N,N-dimethylamine (40% w/v) were purchased from Sigma-Aldrich. All chemicals were used as received without further purification. Deionized water (18.2 MΩ·cm) was obtained from a Milli-Q water purification system.

Characterization. UV/vis/NIR spectra were measured in a quartz cell with an optical path length of 1.0 cm using a Varian Cary50 UV−visible spectrophotometer. Transmission electron microscopy (TEM) was carried out on a Philips 410 microscope operating at 100 kV. TEM samples were prepared by placing a drop of the nanoparticle solution on a carbon-coated 300 mesh Cu grid and allowing it to air-dry.

Synthesis of Silver Nanoprisms. The synthesis of the silver nanoprisms was carried out based on literature procedures.[31] Briefly, 0.050 M $AgNO_3$ (50 μL) was added to deionized water (24.75 mL), followed by the addition of 75 mM trisodium citrate (500 μL), 17.5 mM PVP (100 μL), and H_2O_2 (60 μL). This mixture was stirred for 2 min, after which 0.1 M $NaBH_4$ (250 μL) was added. A change in the color of the solution from yellow to blue was observed after 40 min. The silver nanoprisms were collected by centrifugation at 8,500 rpm (10,000 g) for 3.5 h, and were then redispersed in 5 mM aqueous trisodium citrate (25 mL).

Synthesis of Ag@SiO_2 Core−Shell Nanoprisms. Ag@SiO_2 core shell nanoprisms were prepared according to the synthetic protocol of Xue et al.[32] The nanoprisms were functionalized by the addition of a 5.0 mM ethanolic solution of 16-mercaptohexadecanoic acid; enough solution was added to bring the final thiol concentration to 60 μM. After stirring for 10 min, the functionalized nanoprisms were collected by centrifugation at 8,500 rpm (10,000 g) for 3.5 h, and were redispersed in ethanolic tetraethoxysilane. The entire synthesis procedure was carried in presence of 0.6 M dimethylamine (DMA) using 20% aqueous DMA and stirred for 12 h.

Preparation of TiO_2 and Ag@SiO_2/TiO_2 Pastes. The TiO_2 nanoparticles were synthesized according to literature procedures.[33] Titanium tetraisopropoxide (13 mL) was mixed with glacial acetic acid (2.5 mL) and stirred for 15 min, after which the mixture was poured into deionized water (64 mL) while stirring. After 1 h, 65% nitric acid (1.2 mL) was added into the solution, which was heated to reflux for 80 min with intensive stirring. The prepared colloidal solution was transferred to a 125 mL Teflon-lined autoclave, and heated at 220 °C for 15 h. After completing the autoclave reaction, 65% nitric acid (0.53 mL) was added to the colloidal solution, and the solution homogenized using an ultrasonic horn (QSonica Q500, 1/4″ probe) for 15 min. The TiO_2 nanoparticles were then washed three times with ethanol by centrifugation/redispersion cycles to yield a TiO_2 wet cake.

A paste was prepared from the nanoparticles by adding ethyl cellulose and terpineol. Two kinds of pure ethyl cellulose (EC) powders, EC-10 (Ethocel standard 10 cP, Dow) and EC-45 (Ethocel standard 45 cP, Dow) were dissolved in a 9:7 ratio in ethanol to yield 10% (w/w) solutions. The ethyl cellulose solution, terpineol, and ethanol were added to the TiO_2 wet cake in a 5:4:17.5:1 weight ratio. This mixture was then sonicated using an ultrasonic horn for 15 min (2 s pulses, with a 2 s rest between pulses). The solvent was removed by evaporation under reduced pressure to yield a 13% (w/w) TiO_2 paste.

Ag@SiO_2 incorporated TiO_2 pastes were prepared in the same manner as the pure TiO_2 paste. Ag@SiO_2 particles were added to the TiO_2 wet cake in ratios ranging from 0.01% to 1.0% (w/w). Higher Ag@SiO_2 loadings resulted in more deeply colored pastes.

Cell Fabrication and Characterization. FTO-coated glass (TEC 8, Hartford Glass Co.) was used as a substrate for both the working and the counter electrode. The working electrode was prepared by doctor blading the TiO_2 paste onto a $TiCl_4$ pretreated (0.2 mM(aq), 30 min at 70 °C) FTO-coated glass substrate, followed by sintering at 450 °C in air for 30 min. The thickness of the resulting films was measured using a KLA Tencor D-120 Stylus profilometer, which was calibrated using a 4.474 μm reference sample (VLSI Standard Incorporated, KTS-4.5 QS). The working electrode was then post-treated with $TiCl_4$ (0.2 mM(aq), 30 min at 70 °C) and again sintered at 450 °C. After cooling to 80 °C, the electrode was collected and immersed in dye solution (0.5 mM in EtOH) for 2 days. Counter-electrodes were prepared by spreading two drops of H_2PtCl_6 solution (50 mM in iso-propanol) onto a prepierced (two holes) piece of FTO-coated glass, followed by heating to 380 °C for 30 min. The TiO_2 anode and the counter-electrode were assembled into a sandwich-type cell and sealed with a thermoplastic sealant (Meltonix 1170−25, Solaronix) of 25 μm
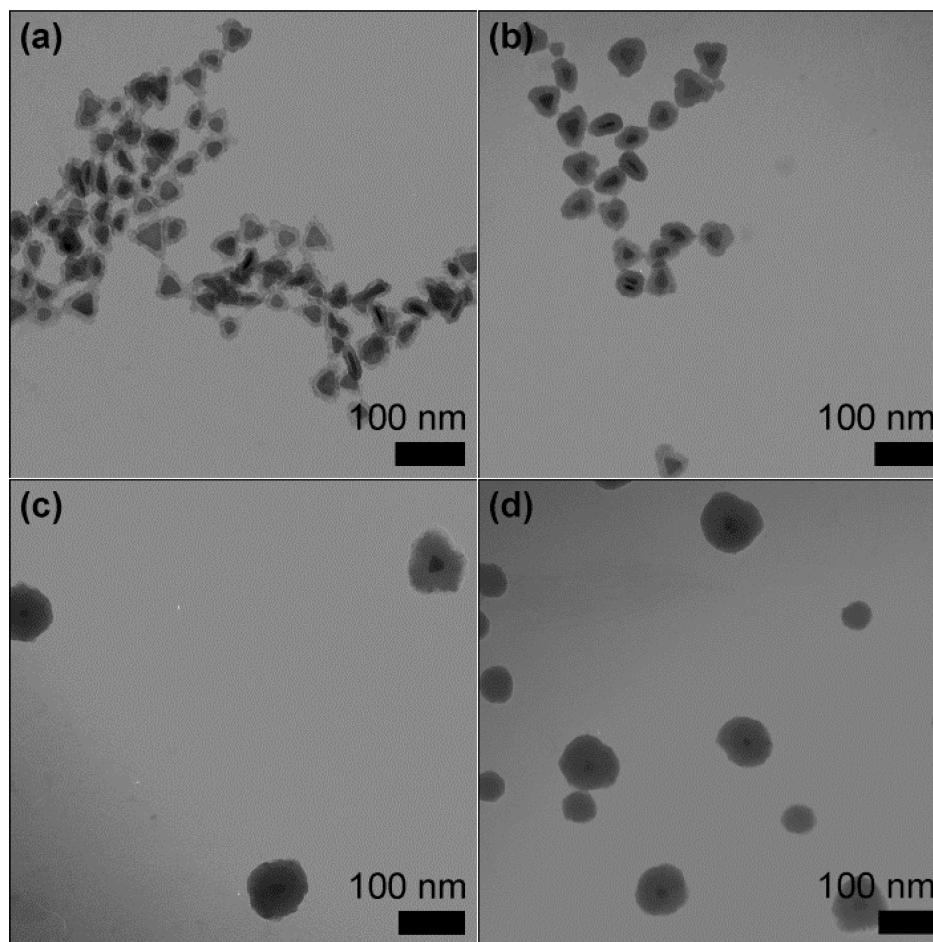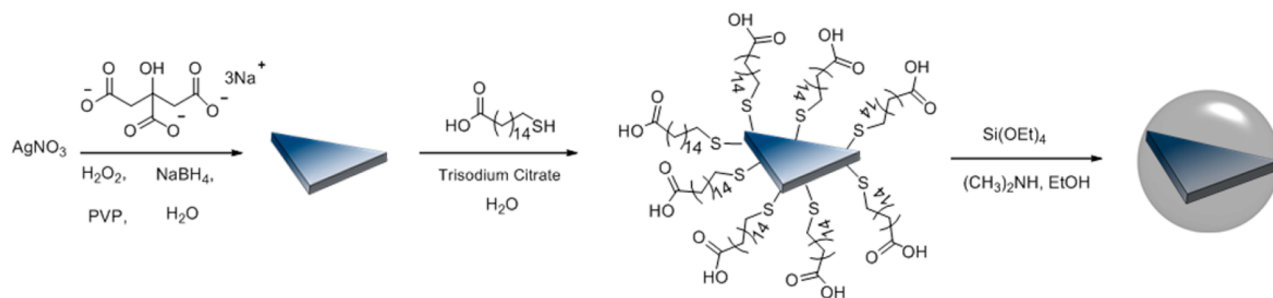
Scheme 1. Synthesis of the Ag@SiO$_2$ Triangular Nanoprisms

Figure 1. TEM micrographs of Ag@SiO$_2$ core−shell particles synthesized with different TEOS concentrations: (a) 0.8 mM, (b) 1.8 mM, (c) 9 mM, and (d) 16 mM.

thickness by hot-pressing at 150 °C for 20 s. The I$^-$/I$_3^-$-based electrolyte (Iodolyte AN-50, Solaronix) was injected through the holes in the counter-electrode, and then sealed using the thermoplastic sealant and cover glass.

The J−V testing of the DSSC sample was carried out using a Keithley 2400 source measure unit. Air mass 1.5 global simulated sunlight (100 mW·cm^{-2}) was produced by a 450 W solar simulator (Sol3A, Oriel Instruments). The incident light intensity was calibrated to one sun by a photovoltaic reference cell system (91150 V, Oriel Instruments). The cell active area was defined as 0.196 cm^2 using a black anodized aluminum aperture mask. IPCE spectra were measured in DC mode using a QE−PV-SI system (Oriel Instruments) equipped with a 300 W xenon arc lamp, filter wheel, and monochromator. The IPCE spectra were calibrated to a silicon reference photodiode (71674, Oriel Instruments).

■ RESULTS AND DISCUSSION

The synthesis of the core−shell Ag@SiO$_2$ nanoprisms is shown in Scheme 1. The triangular silver nanoprism core is first prepared by the chemical reduction of silver nitrate with NaBH$_4$ in the presence of sodium citrate, hydrogen peroxide, and poly(N-vinylpyrrolidone) (PVP).[31] TEM images of the as-prepared nanoprisms are shown in Supporting Information, Figure S1, and the edge length and thickness of the prisms were found to be 30 ± 8 nm and 2.9 ± 0.6 nm, respectively. The particle size distributions are shown in Supporting Information, Figure S2. The nanoprisms have a broad LSPR absorption band centered at 693 nm (Supporting Information, Figure S3). This peak is strongly red-shifted compared with that of spherical silver nanoparticles because of the high aspect ratio of the

nanoprisms. Previous work has assigned the shoulder at 490 nm to an in-plane quadrupole resonance.[34,35] After synthesis, the nanoprisms are functionalized with 16-mercaptohexadecanoic acid, and a silica shell is grown via a sol−gel process using a solution of tetraethylorthosilicate (TEOS) and N,N-dimethylamine in ethanol.[32] The thickness of the silica shell can be tuned by adjusting the concentration of TEOS in the reaction mixture;[32] starting from a single batch of silver nanoprisms, we prepared a series of four samples with shell thicknesses ranging from 7 to 33 nm (Figure 1). In all cases, the nanoprism core (which is distinguishable from the silica shell because of the higher electron contrast of silver) clearly retains its triangular shape. At the lowest TEOS concentration (0.8 mM), a very thin (7 nm) silica shell is visible on the particle surface; as the concentration of TEOS in the reaction mixture is increased, the shell increases in thickness, and the overall shape of the core−shell particle changes from triangular to roughly spherical. At a TEOS concentration of 16 mM, secondary nucleation of silica particles begins to occur, and SiO_2 nanospheres not containing a silver core are observed alongside the core−shell particles. At this TEOS concentration, a 33 nm thick shell is produced; because of the issue of secondary nucleation, this was taken as the upper limit of shell thickness in this study.

The position of the LSPR depends very strongly on the dielectric environment surrounding the nanoparticle. Compared to the citrate-stabilized nanoprisms, the silver nanoprisms functionalized with 16-mercaptohexadecanoic acid show a 10 nm red-shift in the position of the plasmon band (Supporting Information, Figure S3), consistent with thiol-coordination to the surface. After growth of the silica shell, the plasmon peak is further red-shifted with respect to the thiol-functionalized nanoprisms (Figure 2). The magnitude of this red-shift was found to increase with the concentration of TEOS in the reaction mixture, and it tracks the silica shell thickness closely, as would be expected for an increase in the refractive index of the surrounding medium. After the shell has reached 24 nm in thickness, there appears to be little further shift in the peak position, even with further increases in shell thickness. The local field generated by LSPRs is strongly dependent on the distance from the nanoparticle surface.[4,34,35] In the case of the $Ag@SiO_2$ nanoprisms, as the shell thickness increases, the effect of the solvent medium (ethanol) on the LSPR decreases. After the shell thickness has reached a limiting value, the effect of the surrounding medium completely vanishes, and no further red-shift in the LSPR peak is observed. Very similar approaches have been used in the past to measure the distance dependence of the local electromagnetic field,[36−38] and our results suggest that for the thickest silica shells, the position of the plasmon band will remain constant, regardless of its inclusion in the matrix of the TiO_2 photoanode. This also provides a unique opportunity to probe the importance of far-field effects on device efficiency, as for silica shell thicknesses greater than 24 nm, near-field effects should be greatly attenuated, and only resonant scattering (far-field) effects should be observed.

To carry out optimization studies on the incorporation of $Ag@SiO_2$ nanoparticles into DSSCs, the nanoprisms with the thickest (33 nm) silica shell were chosen. These particles were found to be ∼70 nm in diameter (Figure 1d), and while somewhat larger in size than the TiO_2 nanoparticles (d ∼ 20 nm) made via a sol−gel/hydrothermal approach,[33] the two materials could readily be dispersed into a homogeneous paste. This was accomplished by blending the two types of nanoparticles together in various mass ratios, along with ethyl
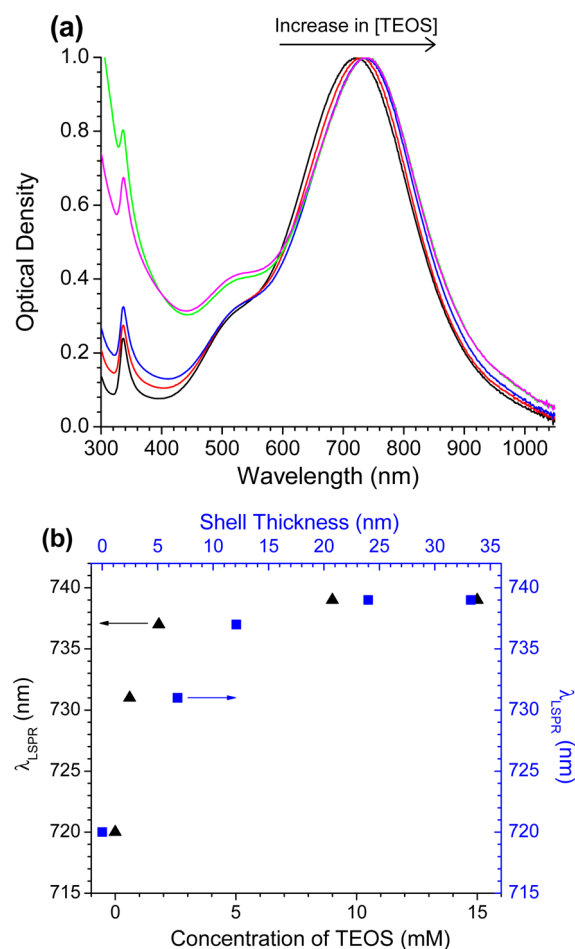

Figure 2. (a) Normalized UV/vis/NIR spectra of Ag nanoprisms functionalized with 16-mercaptohexadecanoic acid (black line), and $Ag@SiO_2$ nanoprisms synthesized using various TEOS concentrations: 0.8 mM (red line), 1.8 mM (blue line), 9 mM (green line), and 16 mM (pink line). (b) Peak position of the LSPR band (λ_{LSPR}) as a function of both TEOS concentration (black triangles) and shell thickness (blue squares).

cellulose binders, followed by ultrasonication for a period of 15 min. After the homogenization process, an opaque blue paste was obtained. The concentration of the $Ag@SiO_2$ nanoparticles in the paste is a key parameter affecting the PCE of the device, since for very low concentrations of $Ag@SiO_2$, little to no effect should be observed, while very high concentrations of the insulating nanoprisms will likely prove detrimental to charge transport within the photoanode. Thus, to determine the optimum mass ratio of $Ag@SiO_2$ to TiO_2, different TiO_2 pastes were prepared with varying concentrations of silver nanoprisms. The $Ag@SiO_2$ to TiO_2 mass ratio of these pastes ranged from 0.01% to 1% (w/w). The pastes were subsequently used to prepare photoanodes that were 8−10 μm in thickness, which were in turn sensitized by N719 dye (Supporting Information, Figure S4). For comparison, control devices were also prepared without inclusion of the $Ag@SiO_2$ nanoprisms.

The J−V curves of both the TiO_2 and the $Ag@SiO_2/TiO_2$-based devices are shown in Figure 3a, and the average open circuit voltages (V_{oc}), short circuit current densities (J_{sc}), fill factors (FF), and PCEs are plotted in Figure 3b as a function of $Ag@SiO_2$ loading. The averaged data are also tabulated in Table 1, along with the PCE of the highest performing device from each set. The control devices (with no plasmonic
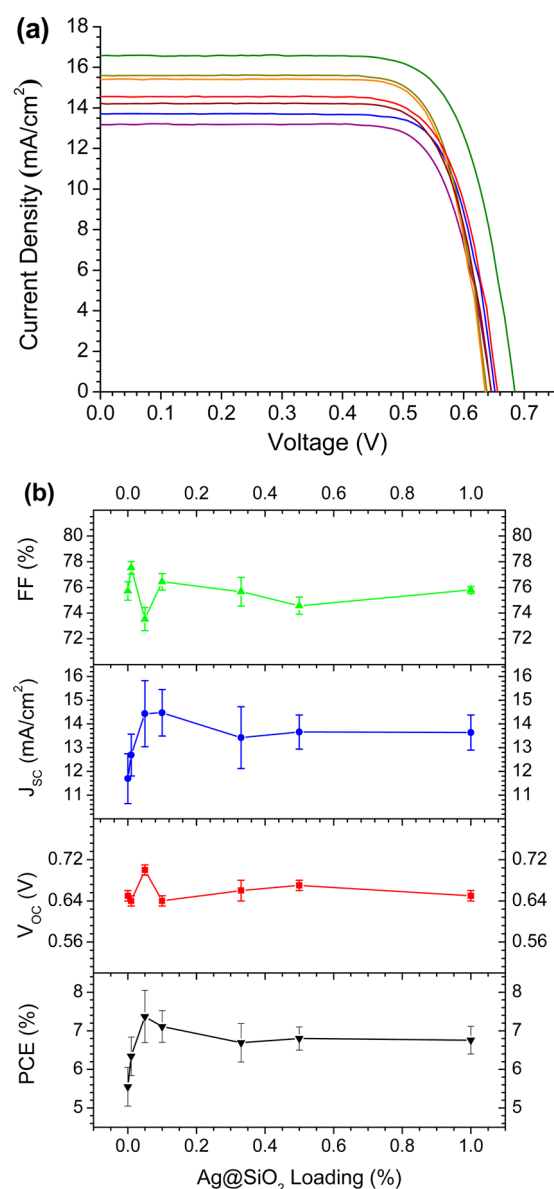
Figure 3. (a) Current–voltage (J–V) characteristics of the highest performing DSSC for each Ag@SiO₂/TiO₂ ratio: 0.00% (purple line), 0.01% (blue line), 0.05% (green line), 0.10% (yellow line), 0.33% (orange line), 0.50% (red line), 1.00% (dark red line). (b) Mean fill factor, short circuit current density, open circuit voltage, and PCE plotted as a function of Ag@SiO₂ loading. The error bars show plus or minus one standard deviation from the mean.

nanoparticles) demonstrated an average PCE of 5.6%. With the addition of 0.01% Ag@SiO₂ to the photoanode, the average PCE increased slightly to 6.3%, and then increased sharply to a maximum of 7.4% with the addition of 0.05% Ag@SiO₂. Thereafter, the average PCE decreased slowly with increased Ag@SiO₂ loading. For the optimized loading of 0.05%, the PCE was improved by $32 \pm 17\%$ relative to the TiO₂ control devices. This is a substantial improvement of device performance, and is especially significant given the very low loading of Ag@SiO₂ required to achieve this performance increase. Even for unoptimized loadings (>0.1%), the devices still displayed PCEs that were 10% higher than the TiO₂ controls. Compared to previous work on DSSCs enhanced by spherical Ag@TiO₂ nanoparticles,[19] the optimized loading of plasmonic nano-particles is substantially reduced while maintaining similar improvements in the overall PCE. Past the optimized loading of 0.05%, there is a clear downward trend in PCE with increasing Ag@SiO₂ concentration. At these concentrations, improve-ments in the PCE due to plasmonic light trapping effects may begin to be offset by a reduction in electron transport pathways within the TiO₂ nanoparticle network.

To statistically validate the results, the data shown in Table 1 was subjected to several statistical tests of significance. In the first of these, an analysis of variance (or ANOVA) test, the data is treated collectively and analyzed for differences between the group means. The results of the ANOVA analysis (at 95% confidence) are shown in Supporting Information, Table S1. In short, the calculated F-value is larger than the critical F-value required for 95% confidence, meaning that the PCE is affected by the Ag@SiO₂ loading in a statistically significant way. While the ANOVA analysis is perhaps most applicable for data sets containing multiple groups (as in the present case), the results are also in very good agreement with those of pairwise t-tests between the plasmon-enhanced cells and the TiO₂ controls (Supporting Information, Table S2), with p-values <0.05. The pairwise t-tests are analogous to the Z-test advocated by Luber and Buriak;[39] however, for the sample sizes involved ($N < 30$), the t-test is more rigorous.

From Figure 3b, it is clear that the overall increase in PCE is driven by improvements in J_{sc}. Compared to the TiO₂ control devices, only small changes to the open circuit voltage and fill factor were observed for any of the plasmonic devices (a maximum difference of 6% and 3%, respectively). Furthermore, there is no consistent trend observed for either the V_{oc} or FF, with various Ag@SiO₂ loadings producing both positive and negative changes, and some loadings leading to no change at all. Clearly, neither the V_{oc} nor the FF can be responsible for the $32 \pm 17\%$ increase in PCE. In contrast, when 0.05% Ag@SiO₂ is incorporated into the device, the J_{sc} increases from 11.2 to 14.4

Table 1. Mean V_{oc}, J_{sc}, FF, and PCE, along with Their Associated Standard Deviations, for DSSCs with Different Ag@SiO₂ Loadings[a]

Ag@SiO₂ loading (%)	average V_{oc} (V)	average J_{sc} (mA/cm2)	average FF (%)	average PCE (%)	best PCE (%)	N
0.00	0.65 ± 0.01	11.2 ± 1.2	75.7 ± 1.2	5.6 ± 0.6	6.5	15
0.01	0.64 ± 0.01	12.7 ± 0.9	77.5 ± 0.5	6.3 ± 0.5	6.9	4
0.05	0.70 ± 0.01	14.4 ± 1.4	73.5 ± 0.9	7.4 ± 0.7	8.4	13
0.10	0.64 ± 0.01	14.5 ± 1.0	76.4 ± 0.6	7.1 ± 0.4	7.3	4
0.33	0.66 ± 0.02	13.4 ± 1.3	75.6 ± 1.1	6.7 ± 0.5	7.5	6
0.50	0.67 ± 0.01	13.7 ± 0.7	74.6 ± 0.7	6.8 ± 0.3	7.1	4
1.00	0.65 ± 0.01	13.6 ± 0.7	75.8 ± 0.3	6.8 ± 0.4	7.0	4

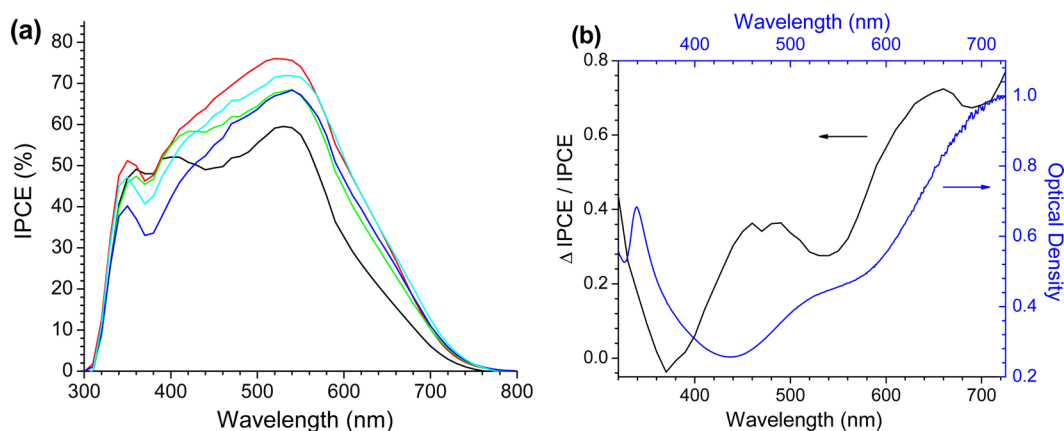[a]The number of devices tested (N) for each loading is shown.

Figure 4. (a) IPCE spectra of DSSCs made using various Ag@SiO$_2$/TiO$_2$ ratios: 0.0% (black line), 0.05% (red line), 0.10% (cyan line), 0.33% (green line), and 0.5% (blue line). (b) The relative IPCE enhancement ((IPCE$_{Ag@SiO2}$ − IPCE$_{control}$)/IPCE$_{control}$) for the device with a 0.05% Ag@SiO$_2$ (black line) loading and the absorption spectrum of the Ag@SiO$_2$ nanoprisms (blue line).

mA/cm^2, and then drops slowly for large Ag@SiO$_2$ loadings, mirroring the trends observed in the PCE. These data are entirely consistent with plasmonic light trapping being the primary driving force behind the increase in PCE. Increased LHE results in improved currents, but should have no effect on either V_{oc} or FF. While previous work on DSSCs incorporating Au@TiO$_2$ has suggested that electron charging effects may result in shifts of the quasi-Fermi level of the TiO$_2$ (and hence changes to the V_{oc}),[25] the insulating SiO$_2$ shell used in the present work should only permit changes to the LHE.

To confirm the origin of these improvements in PCE, IPCE measurements were carried out on a number of the completed devices (Figure 4). Since the current density in a solar cell is governed by the integral of the product of the photon flux and the IPCE, any changes to the value of J_{sc} should also be reflected in the IPCE spectra. The results agree well with the trends observed in the $J-V$ curves. DSSCs with a 0.05% loading of Ag@SiO$_2$ nanoprisms displayed notably higher IPCE values in the range of wavelengths from 400 to 750 nm compared to the reference device. The IPCE increased from 60% to 76% at 530 nm (the maximum of the IPCE spectrum), and substantial increases were also observed at longer wavelengths as well (e.g., from 23% to 39% at 630 nm). While it is also possible for pure silica nanoparticles to scatter light (and therefore produce higher values of J_{sc} and IPCE), if that were the case one would expect to see dramatically different behavior in the IPCE spectra. Smaller nanoparticles ($d < 0.1$ λ) should produce enhancements in the IPCE spectrum that closely follow the $1/\lambda^4$ dependence typical of Rayleigh scattering, while larger nanoparticles ($d \gg 0.1$ λ) should lead to scattering that is largely independent of wavelength. The observed differences in the IPCE spectrum (Supporting Information, Figure S5) are inconsistent with either scenario, but entirely consistent with resonant scattering caused by the Ag@SiO$_2$ nanoparticles.

As the Ag@SiO$_2$ concentration increases, there continues to be an improvement in IPCE for the long wavelength region of the spectrum, despite a decrease in IPCE at shorter wavelengths. This spectral shift can best be understood by separately considering the various factors that control the IPCE, including the LHE, the efficiency of electron injection from the excited dye molecule to the TiO$_2$ electrode, and the electron collection efficiency at the anode. The increase in IPCE at wavelengths resonant with the Ag@SiO$_2$ LSPR band is consistent with an increase in the LHE. For wavelengths off-

resonance with the LSPR band, however, the Ag@SiO$_2$ nanoparticles are expected to have a detrimental impact on the IPCE. Embedding insulating silica particles inside the mesoporous TiO$_2$ network will disrupt charge percolation networks, forcing the charge carriers to take increasingly convoluted pathways to the electrode as the Ag@SiO$_2$ concentration is increased. Several reports have clearly demonstrated that straighter, less convoluted electron transport pathways with fewer grain boundaries are critical in maximizing the electron collection efficiency.[40−42] As such, the decrease in collection efficiency results in a net decrease in the IPCE for wavelengths that are off-resonance with the LSPR band, and these effects are particularly pronounced for the devices with the highest Ag@SiO$_2$ loadings.

Further evidence for the contribution of the silver nanoprisms to the enhanced LHE can be found by comparison of the relative increase in IPCE (Δ_{IPCE}/IPCE$_{control}$) and the Ag@SiO$_2$ absorption spectrum (Figure 4b). The IPCE enhancement spectrum is dominated by a large feature at 660 nm, with a second, less pronounced peak at 460 nm. This is in reasonable agreement with the Ag@SiO$_2$ absorption spectrum, which displays an intense peak at 724 nm due to the in-plane dipole LSPR mode, and a shoulder at 515 nm due to the in-plane quadrupole mode (note that the position of this peak is slightly offset from the data shown in Figure 2 because of batch-to-batch variability in the preparation of the nanoprisms). This correlation between the nanoparticle LSPR band and the IPCE enhancement spectrum is in agreement with previous reports of plasmon-enhanced DSSCs.[19,43] There are two notable differences between the two spectra: first, the location of the IPCE enhancement is blue-shifted with respect to the initial absorption spectrum of the Ag@SiO$_2$ nanoparticles, and second, there is an additional contribution at 460 nm that is unlikely to be entirely due to the quadrupole mode of the nanoprisms. These discrepancies may be caused by changes in the particle shape during the electrode deposition and/or cell fabrication process (most likely during the sintering step). To evaluate their stability, TEM images were acquired after sintering a sample of Ag@SiO$_2$ nanoparticles (Supporting Information, Figure S6). The tips of triangular silver nanoprisms are prone to rounding or truncation (thereby blue-shifting the LSPR band),[44] and various levels of tip rounding can be seen in Supporting Information, Figure S6. Some particles are still triangular in shape (giving rise to the
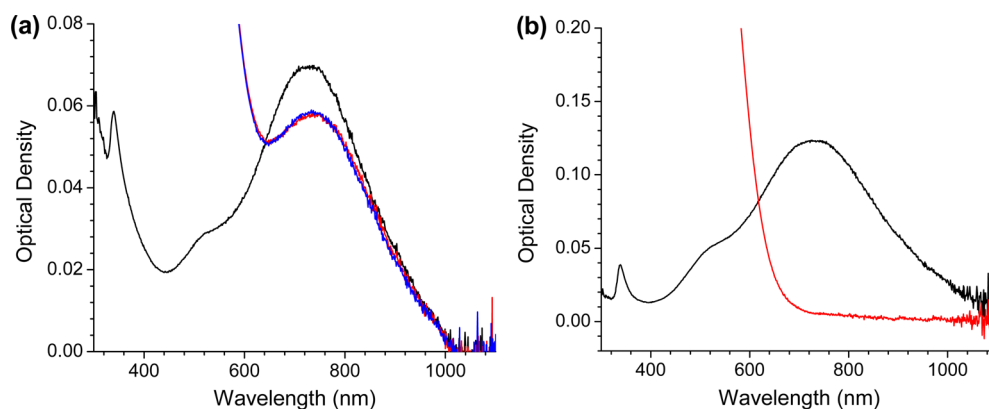
Figure 5. (a) UV/vis/NIR spectra of the Ag@SiO$_2$ nanoprisms with a 33 nm thick shell: in acetonitrile (black line), 30 min after adding the I$^-$/I$_3^-$ electrolyte (red line), and 20 h after addition of the electrolyte solution (blue line). (b) UV/vis/NIR spectra of the Ag@SiO$_2$ nanoprisms with a 7 nm thick shell: in acetonitrile (black line), and 30 min after adding the I$^-$/I$_3^-$ electrolyte (red line).

enhancements observed at wavelengths >600 nm), while others have been reduced in size to smaller plates or spheres (likely contributing to the extra IPCE enhancement observed at 460 nm). The complete retention of anisotropic nanoparticle shape under sintering conditions is a challenge for many in this area, and is certainly an area in which further improvements could be made; however, regardless of any small changes in particle morphology, the LHE of the DSSC has been dramatically improved in the vicinity of 660 nm—a spectral region that is very challenging to reach with isotropic, spherical nanoparticles.

To investigate the effect of silica shell thickness on the plasmon-based efficiency enhancement, Ag@SiO$_2$ nanoparticles with various shell thicknesses were incorporated into DSSCs. Nanoparticles with SiO$_2$ shells of 7 nm were chosen to provide a contrast with the thick-shelled nanoprisms studied previously; since near-field effects are strongly distance dependent, thin silica shells might be expected to lead to greater overall improvements. Our results indicate that the efficiencies of DSSCs fabricated with the thin-shelled nanoprisms are no different than the PCEs of the TiO$_2$ controls (Supporting Information, Figure S7), in stark contrast to the improvements in PCE observed for the thick-shelled nanoprisms. To better understand this discrepancy, the stabilities of both types of Ag@SiO$_2$ core−shell particles were tested in I$^-$/I$_3^-$ electrolyte solutions over a period of 20 h. The Ag@SiO$_2$ nanoparticles with the thickest shells showed no change in either the intensity or the position of the plasmon band after electrolyte exposure; however, the Ag@SiO$_2$ nanoparticles with the 7 nm silica shells suffered an immediate (within 30 min) disappearance of the LSPR band (Figure 5). This clearly indicates that the thinner silica shell is either incomplete or slightly porous, leading to dissolution of the underlying silver nanoprism core.

CONCLUSIONS

We have demonstrated the successful utilization of triangular silver nanoprisms as light harvesting elements in a DSSC. The loading of the silica-capped nanoprisms was optimized, and it was found that a very low loading of 0.05% Ag@SiO$_2$ in the titania photoanode resulted in a 32 ± 17% increase in the overall PCE of the device, driven primarily by an increase in the short circuit current density. This plasmonic efficiency enhancement resulted in an 8.4% PCE for the highest performing device in the present study.

IPCE measurements clearly indicate that these increases are due to improvements in the LHE at longer wavelengths

(resonant with the Ag@SiO$_2$ LSPR band), and that further increases in the Ag@SiO$_2$ loading result in a detrimental effect on the electron collection efficiency. In contrast to previous work on spherical nanoparticle systems, the anisotropic nature and high aspect ratio of the nanoprism core leads to strongly red-shifted LSPR modes and large improvements in the LHE at longer wavelengths. We expect that the application of anisotropic metal particles to plasmon-enhanced DSSCs will help fulfill an important role in improving the efficiency of these devices, namely, the improvement of the LHE at red to NIR wavelengths where most dyes absorb very weakly.

■ ASSOCIATED CONTENT

S **Supporting Information**
TEM images of as-prepared silver nanoprisms, UV/vis/NIR spectra of silver nanoprisms before and after functionalization with 16-mercaptohexadecanoic acid, results of statistical tests, TEM image of nanoprisms after sintering, tabulated device parameters for DSSCs prepared using the thin-shelled Ag@SiO$_2$ nanoprisms. This material is available free of charge via the Internet at http://pubs.acs.org.

■ AUTHOR INFORMATION

Corresponding Author
*E-mail: tim.kelly@usask.ca.

Author Contributions
†These authors contributed equally to this work.

Notes
The authors declare no competing financial interest.

■ REFERENCES

(1) Yella, A.; Lee, H. W.; Tsao, H. N.; Yi, C.; Chandiran, A. K.; Nazeeruddin, M. K.; Diau, E. W.; Yeh, C. Y.; Zakeeruddin, S. M.; Grätzel, M. *Science* **2011**, *334*, 629−634.

11050

dx.doi.org/10.1021/am403280r | *ACS Appl. Mater. Interfaces* 2013, 5, 11044−11051

(2) Hagfeldt, A.; Boschloo, G.; Sun, L.; Kloo, L.; Pettersson, H. *Chem. Rev.* **2010**, *110*, 6595−6663.

(3) Grätzel, M. *Acc. Chem. Res.* **2009**, *42*, 1788−1798.

(4) Hamann, T. W.; Jensen, R. A.; Martinson, A. B. F.; Van Ryswyk, H.; Hupp, J. T. *Energy Environ. Sci.* **2008**, *1*, 66−78.

(5) Campbell, W. M.; Jolley, K. W.; Wagner, P.; Wagner, K.; Walsh, P. J.; Gordon, K. C.; Schmidt-Mende, L.; Nazeeruddin, M. K.; Wang, Q.; Grätzel, M.; Officer, D. L. *J. Phys. Chem. C* **2007**, *111*, 11760−11762.

(6) Li, L.-L.; Diau, E. W.-G. *Chem. Soc. Rev.* **2013**, *42*, 291−304.

(7) Balraju, P.; Suresh, P.; Kumar, M.; Roy, M. S.; Sharma, G. D. *J. Photochem. Photobiol., A* **2009**, *206*, 53−63.

(8) Hore, S.; Vetter, C.; Kern, R.; Smit, H.; Hinsch, A. *Sol. Energy Mater. Sol. Cells* **2006**, *90*, 1176−1188.

(9) Zheng, Y.-Z.; Tao, X.; Wang, L.-X.; Xu, H.; Hou, Q.; Zhou, W.-L.; Chen, J.-F. *Chem. Mater.* **2009**, *22*, 928−934.

(10) Huang, F.; Chen, D.; Zhang, X. L.; Caruso, R. A.; Cheng, Y.-B. *Adv. Funct. Mater.* **2010**, *20*, 1301−1305.

(11) Ding, I. K.; Zhu, J.; Cai, W.; Moon, S.-J.; Cai, N.; Wang, P.; Zakeeruddin, S. M.; Grätzel, M.; Brongersma, M. L.; Cui, Y.; McGehee, M. D. *Adv. Energy Mater.* **2011**, *1*, 52−57.

(12) Ko, D.-H.; Tumbleston, J. R.; Gadisa, A.; Aryal, M.; Liu, Y.; Lopez, R.; Samulski, E. T. *J. Mater. Chem.* **2011**, *21*, 16293−16303.

(13) Linic, S.; Christopher, P.; Ingram, D. B. *Nat. Mater.* **2011**, *10*, 911−921.

(14) Ozbay, E. *Science* **2006**, *311*, 189−193.

(15) Jain, P. K.; Lee, K. S.; El-Sayed, I. H.; El-Sayed, M. A. *J. Phys. Chem. B* **2006**, *110*, 7238−7248.

(16) Jain, P. K.; Huang, X.; El-Sayed, I. H.; El-Sayed, M. A. *Acc. Chem. Res.* **2008**, *41*, 1578−1586.

(17) Atwater, H. A.; Polman, A. *Nat. Mater.* **2010**, *9*, 205−213.

(18) Hou, W. B.; Pavaskar, P.; Liu, Z. W.; Theiss, J.; Aykol, M.; Cronin, S. B. *Energy Environ. Sci.* **2011**, *4*, 4650−4655.

(19) Qi, J. F.; Dang, X. N.; Hammond, P. T.; Belcher, A. M. *ACS Nano* **2011**, *5*, 7108−7116.

(20) Brown, M. D.; Suteewong, T.; Kumar, R. S. S.; D'Innocenzo, V.; Petrozza, A.; Lee, M. M.; Wiesner, U.; Snaith, H. J. *Nano Lett.* **2011**, *11*, 438−445.

(21) Standridge, S. D.; Schatz, G. C.; Hupp, J. T. *J. Am. Chem. Soc.* **2009**, *131*, 8407−8409.

(22) Jeong, N. C.; Prasittichai, C.; Hupp, J. T. *Langmuir* **2011**, *27*, 14609−14614.

(23) Chang, S.; Li, Q.; Xiao, X. D.; Wong, K. Y.; Chen, T. *Energy Environ. Sci.* **2012**, *5*, 9444−9448.

(24) Standridge, S. D.; Schatz, G. C.; Hupp, J. T. *Langmuir* **2009**, *25*, 2596−2600.

(25) Choi, H.; Chen, W. T.; Kamat, P. V. *ACS Nano* **2012**, *6*, 4418−4427.

(26) Sheehan, S. W.; Noh, H.; Brudvig, G. W.; Cao, H.; Schmuttenmaer, C. A. *J. Phys. Chem. C* **2012**, *117*, 927−934.

(27) Aherne, D.; Ledwith, D. M.; Kelly, J. M. Synthesis of Anisotropic Noble Metal Nanoparticles. In *Metal-Enhanced Fluorescence*; John Wiley & Sons, Inc.: Hoboken, NJ, 2010; pp 295−362.

(28) Aherne, D.; Ledwith, D. M.; Gara, M.; Kelly, J. M. *Adv. Funct. Mater.* **2008**, *18*, 2005−2016.

(29) Janković, V.; Yang, Y.; You, J.; Dou, L.; Liu, Y.; Cheung, P.; Chang, J. P. *ACS Nano* **2013**, *7*, 3815−3822.

(30) Kulkarni, A. P.; Noone, K. M.; Munechika, K.; Guyer, S. R.; Ginger, D. S. *Nano Lett.* **2010**, *10*, 1501−1505.

(31) Zhang, Q.; Li, N.; Goebl, J.; Lu, Z.; Yin, Y. *J. Am. Chem. Soc.* **2011**, *133*, 18931−18939.

(32) Xue, C.; Chen, X.; Hurst, S. J.; Mirkin, C. A. *Adv. Mater.* **2007**, *19*, 4071−4074.

(33) Ito, S.; Murakami, T. N.; Comte, P.; Liska, P.; Grätzel, C.; Nazeeruddin, M. K.; Grätzel, M. *Thin Solid Films* **2008**, *516*, 4613−4619.

(34) Kelly, K. L.; Coronado, E.; Zhao, L. L.; Schatz, G. C. *J. Phys. Chem. B* **2003**, *107*, 668−677.

(35) Evanoff, D. D., Jr.; Chumanov, G. *ChemPhysChem.* **2005**, *6*, 1221−1231.

(36) Evanoff, D. D.; White, R. L.; Chumanov, G. *J. Phys. Chem. B* **2004**, *108*, 1522−1524.

(37) Haes, A. J.; Zou, S.; Schatz, G. C.; Van Duyne, R. P. *J. Phys. Chem. B* **2003**, *108*, 109−116.

(38) Rodríguez-Fernández, J.; Pastoriza-Santos, I.; Pérez-Juste, J.; García de Abajo, F. J.; Liz-Marzán, L. M. *J. Phys. Chem. C* **2007**, *111*, 13361−13366.

(39) Luber, E. J.; Buriak, J. M. *ACS Nano* **2013**, *7*, 4708−4714.

(40) Kang, S. H.; Choi, S. H.; Kang, M. S.; Kim, J. Y.; Kim, H. S.; Hyeon, T.; Sung, Y. E. *Adv. Mater.* **2008**, *20*, 54−58.

(41) Ghadiri, E.; Taghavinia, N.; Zakeeruddin, S. M.; Grätzel, M.; Moser, J.-E. *Nano Lett.* **2010**, *10*, 1632−1638.

(42) Wong, D. K.-P.; Ku, C.-H.; Chen, Y.-R.; Chen, G.-R.; Wu, J.-J. *ChemPhysChem* **2009**, *10*, 2698−2702.

(43) Dang, X.; Qi, J.; Klug, M. T.; Chen, P.-Y.; Yun, D. S.; Fang, N. X.; Hammond, P. T.; Belcher, A. M. *Nano Lett.* **2013**, *13*, 637−642.

(44) Sherry, L. J.; Jin, R.; Mirkin, C. A.; Schatz, G. C.; Van Duyne, R. P. *Nano Lett.* **2006**, *6*, 2060−2065.